Journal of Materials Chemistry A

ARTICLE

Theoretical and Experimental Studies of Highly Active Graphene Nanosheets to determine Catalytic Nitrogen Sites Responsible for the Oxygen Reduction Reaction in Alkaline Media

J. Vazquez-Arenas[a,†], A. Galano[a], D. Un Lee[b], D. Higgins[b], A. Guevara-García[a], Z. Chen[b]

Graphene nanosheets with heterogeneously doped nitrogen atoms are synthetized using a facile one-step method based on extremely rapid heating (temperature ramps ≥ 150 °C s⁻¹). Raman and X-ray photoelectron spectroscopy reveal efficacious nitrogen incorporation into the graphitic network. A half-cell testing conducted in alkaline media with a rotating disk electrode technique shows that the N-doped graphene nanosheets present a very comparable Oxygen Reduction Reaction (ORR) activity to the state-of-the-art commercial 20 wt% Pt/C catalyst. The outstanding catalytic activity of metal-free carbon-based graphene nanosheets is ascribed to the opened structure produced by the facile one-step synthetic procedure resulting in significantly enhanced active site exposure. Density functional theory is used to elucidate the electrochemical properties of these nanosheets on the basis of bandgap, vertical ionization energies, and adsorption free energies of intermediate species ($^\bullet$OOH, ^{3}O, $^\bullet$OH, and $^\bullet$H) formed during the ORR associative mechanism occurring in alkaline media. A systematic analysis is conducted by comparing pristine graphene and N-doped graphene nanosheets of multiple sizes containing single and all together pyridinic, pyrrolic and graphitic species to determine the adequate size of the cluster and the most catalytically active N site to perform the ORR. From all possible adsorption sites for the intermediates including nitrogen on a larger cluster model with 37 rings doped with all type of nitrogen bonding, the adsorption on top of any carbon adjacent to a central graphitic nitrogen represents a significant reduction in the energy barrier of the ORR electrocatalysis. Theoretical calculations of the bond strengths of all possible species show that the removal of ^{3}O species from the electrode surface to form OH$_{ads}$ is the rate-controlling step of the ORR mechanism. Consistently, a surface electrode potential of 0.918 V vs SHE computed for this reaction step is close to 0.867 V vs SHE reported for the second reaction (OOH⁻/OH⁻) of the mechanism with two consecutive 2-electron transfer steps obtained under standard conditions.

Introduction

The development of new cathodes for low temperature fuel cells has spurred the research of low cost and durable materials. Typically, these compounds contain Platinum nanoparticles supported on carbon black having high surface area, as a result of intrinsically sluggish nature of kinetics of ORR on most substrates.[1, 2] The limited natural abundance of platinum, and gradually increasing cost, renders its long term applicability unpractical for commercial purposes. Thus, it has become crucial to investigate non-noble materials displaying a similar performance, in order to minimize the use of platinum.

Non-noble electrocatalysts have been synthetized as alternatives to Pt-based catalysts including enzymatic compounds,[3] metal chalcogenides,[4, 5] metal free graphene and nitrogen doped carbon catalysts (N-CNTs).[6, 7] Metal free graphene nanosheets (GN) have attracted a tremendous attention for energy applications as result of its structure: atomic thick planar sheets of sp2-bonded carbon atoms, densely packed in a 2D honeycomb crystal lattice.[8-11] This crystallographic structure delivers exceptional physical and chemical properties such as high theoretical surface area (2630 m^2 g⁻¹), electrical conductivity (i.e. 106 S cm⁻¹ at room temperature) and chemical/mechanical stability; and the capacity of functionalization and fabrication.[12]

In order to attain adequately high kinetics of ORR,[13-22] the chemical and electronic properties of the GN structure can be modified by nitrogen doping (N-GN), which forms up to five valence bonds with the adjacent carbon atoms having the highest positive charge. This role has been confirmed where more electronegative nitrogen removes electrons from adjacent carbons, which on their turn act as the active site for the ORR.[13-17, 23] The pyridinic nitrogen type (sp^2 hybridization) located at the edges or defects of the GN possesses a localized electron lone pair which highly modifies the local electron density to enhance electrocatalytic reactions. The pyrrolic nitrogen type (sp^3 hybridization) forms part of a five membered ring structure, and the graphitic nitrogen (sp^3 hybridization) results from the carbon substitution by nitrogen in the GN. A

a. Departamento de Química, Universidad Autónoma Metropolitana, San Rafael Atlixco 186, C.P. 09340, México, D.F., México.
b. Department of Chemical Engineering, Waterloo Institute for Nanotechnology, University of Waterloo, 200 University Avenue West, Waterloo, Ontario, Canada N2L 3G1.
† Corresponding author: jgva@xanum.uam.mx, jorge_gva@hotmail.com
Electronic Supplementary Information (ESI) available: [Tables for bond distances and angles]. See DOI: 10.1039/x0xx00000x

Please do not adjust margins

ARTICLE

fourth type of nitrogen identified as oxidized pyridinic has been also found in carbonaceous materials, however, electrocatalytic properties have not been assigned to this species.[24-26] Some studies have reported that the increase of the overall nitrogen content, including typical nitrogen functional groups (graphitic, pyrrolic and pyridinic species, refer to Fig. 1) and edge plane defects deliver higher degree of electrocatalysis compared to traditional Pt-based catalysts.[26, 27] However, there is a controversy since other studies report that N content in excess could actually introduce a large number of defects into the carbonaceous structure, leading to a poor electronic conductivity. To this concern, a more important aspect to consider is the predominance of a nitrogen-bonding type upon the performance of the catalyst for ORR. Ni et al found that all nitrogen species lower the energy barriers for oxygen molecule dissociation, but graphite-like nitrogen (i.e. graphitic) and Stone-Wales defect nitrogen are more effective for this process than pyridine-like nitrogen.[28] Thus, an adequate level of nitrogen bonding with catalytically active species could be more critical than the overall nitrogen content to obtain high performance GN catalysts.

Density functional theory has been successfully used to describe the ORR mechanism on different carbonaceous materials, mainly on the basis of binding energies computed for intermediates formed during the course of ORR.[29-38] Although these studies have been decisive to evaluate the energy barriers arising with N doped carbonaceous structures, they have mostly focused on acidic environments,[29, 31, 33, 35] using platinum (Pt)-based catalysts,[39-43] or nitrogen free Pt/CNTs.[34, 44, 45] In general, alkaline conditions are more favourable from an application standpoint, owing to the significantly more facile ORR kinetics and less corrosive conditions encountered in comparison to acidic conditions. This enables the use of non-precious metal catalysts in alkaline conditions, providing substantial cost savings. In addition, the use of nitrogen-doped nanocarbon electrocatalysts in direct methanol fuel cell (DMFC) operating under alkaline conditions is advantageous due to their high tolerance to methanol which enhances stability.[46-49] However, to our current state of knowledge, only one study has been intended to analyse solvent interactions, surface adsorbates and coverages in alkaline media, determining that the ORR associative mechanism is energetically more favourable than the dissociative one, and where the consumption of O species was the rate-controlling step.[30] Nevertheless, the absence of pyrrolic and pyridinic-type nitrogen species in their computed structures and the excessive amount of overall nitrogen content could hinder crucial information of the ORR under alkaline conditions. Experimentally, it is challenging to control the concentration of a single nitrogen species in N-GN and CNTs.[13-17, 26, 50, 51] Consequently, most catalysts synthesized for ORR should contain pyridinic, pyrrolic, and graphitic nitrogen species as a function of the type and amount of precursor utilized. Nitrogen-doped species have been individually considered in carbonaceous materials, but their combined effects (e.g. electronic, structural, energy barriers) towards ORR activity remain unknown, even for acid conditions.
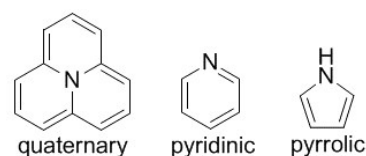

Figure 1 Nitrogen functional groups contained in doped carbonaceous materials, typically related to the ORR electrocatalysis.

Thus, this study aims to evaluate the ORR on N-GN containing pyridinic, pyrrolic and graphitic species in alkaline media. N-GN are experimentally synthesized, and characterized to provide information of the structures of these catalysts, which on its turn is connected to quantum mechanics calculations to compute their properties, as well as the phenomena and interactions involved in the ORR mechanism. The synthesis of the experimental N-GN is carried out by a facile one-step method recently implemented by Lee et al.,[52] which utilizes extremely rapid heating of graphene oxides (GO) from room temperature to temperatures higher than 800 °C within five seconds (temperature ramps ≥ 150 °C s^{-1}). This procedure leads to the removal of most of the evolved gases in a very short period time which helps to maximize the expansion of the graphene nanosheets in order to enhance the ORR electrocatalysis.

In addition, analyses of the ground state N-GN structures are performed based on properties such as bandgap, vertical ionization energies, and the free energies for the adsorption of the intermediate species formed during the ORR associative mechanism in alkaline media. To that purpose the density functional theory (DFT) was used. A comparison is made with the energies of pristine graphene and catalysts with single nitrogen species, in order to highlight the advantages of N doping and the presence of all nitrogen species upon catalysis, respectively. Gibbs free energies for the adsorption processes between the intermediates and the N-GN are computed for multiple possible actives sites, including nitrogen and adjacent carbon atoms, in order to determine the most favourable ORR active sites. The free energy of the most active site is subsequently utilized to calculate the reduction potentials, which are compared against the potential value of an overall two-electron transfer steps obtained under standard conditions.

Experimental

Synthesis of N-Graphene Nanosheets

An extremely rapid heating rate was utilized to synthesize N-GN having highly opened structure, combining thermal reduction and ammonia treatment into a one-step process without using a substrate. The GO used for N-GN preparation was based on a modification of Hummer's method[53] using natural graphite flakes. Multiple synthesis were experimentally conducted to analyse the influence of a slow (5 °C min^{-1}) and a rapid (~150 °C sec^{-1}) heating rate, as well as the temperature at which the synthesis was carried out (800 °C, 900 °C, 1000 °C, and 1100 °C),

upon the degree of expansion of the graphene nanosheets and its effect on the electrochemical performance. These conditions revealed that the N-GN fabricated at 1100 °C using a rapid heating ramp (≥ 150 °C s^{-1}) present an unique open-structured morphology with large interlayer spacing, highly suitable for the electrocatalysis of ORR, whence only these conditions are utilized in the present study. Further details of the complete experimental analysis have been formerly reported by Lee et al.[52]

Structural and Chemical characterization

X-ray diffraction (XRD) was conducted using an AXS D8 Advance, Brunker equipment to investigate the structural modification of the N-GN after synthesis. Raman spectroscopy (LabRAM HR, HORIBA scientific) was used to analyse the graphitic bonds, and X-ray photoelectron spectroscopy (XPS) (K-Alpha XPS spectrometer, Thermal Scientific) was performed to determine the atomic composition of the graphene nanosheets and to quantify the nitrogen species (pyridinic, pyrrolic, and graphitic).

Oxygen Reduction Reaction

The ORR electroactivity of N-GN was tested in 0.1 M KOH using a three-electrode cell: a glassy carbon electrode (diameter: 5 mm) coated with a suspension of 20 uL of 4 mg mL^{-1} N-GN (0.5 wt% Nafion in ethanol) was used as the working electrode (catalytic loading of ca. 0.4 mg cm^{-2}). The electroactivity of this material was compared with a 20 wt% Pt/C coated working electrode prepared on a glassy carbon with the same loading. A saturated Calomel Electrode (SCE) and a platinum wire were utilized as reference and counter electrodes, respectively. All the electrochemical measurements were conducted using a rotating disk electrode (RDE) at room temperature, using a potentiostat (Pine Instrument Co., AFCBP-1).

Computational details

The electronic calculations have been carried out with the package of programs Gaussian 09, Revision D.01.[54] We have used a dual level procedure to calculate the energies of the systems of interest. This strategy has become common in the study of large systems, because it significantly reduces the computational costs, and at the same it usually reproduces the main features of the reaction path correctly. It is known as B//A, and consists of geometry optimizations at a given level (A) followed by single-point calculations (without optimization) at a higher level (B). In the present case the semi-empirical method PM6[55] was chosen as level A, while PBE0/6-31+G(d) corresponds to level B. The reliability of this dual level approach is mainly ruled by the similarity between geometries obtained at both levels of theory. Accordingly, this was tested for some representative cases and the validity of using this particular dual level combination was demonstrated. Therefore, PBE0 energies obtained at the PM6 geometries, are the ones used for the analyses. In addition, cluster models were used instead of periodic ones because pyridinic and pyrrolic sites are terminal,

thus finite models are needed to include these structural features.

PM6 was chosen for geometry optimizations because of the large size, and number, of the studied systems, which leads to high computationally demanding calculations. This semi-empirical method has been proven to be superior to other semi-empirical quantum mechanical (QM) methods in various aspects, including geometries.[55, 56] In fact, it has been proposed that PM6 currently represents the state of the art in the development of semi-empirical QM methods.[56]

Validation of PM6 geometry optimizations

Since PM6 has been used for geometry optimizations in this work, we have tested its reliability for this purpose using model systems of similar nature to those involved in the presented investigation. They are of two different sizes, comprising 7 and 19 hexagonal rings (R7 and R19, respectively) including, separately or simultaneously, the different types of N sites investigated in this work (graphitic, pyridinic, and pyrrolic). Selected geometrical parameters, representative of the whole system have been analysed. They are bond distance and bond angles involving the atoms highlighted in Fig. 2.

It was found that the parameters obtained from PM6 calculations are in very good agreement with those obtained at PBE0/6-31+G(d) level of theory (Supporting Information, Tables
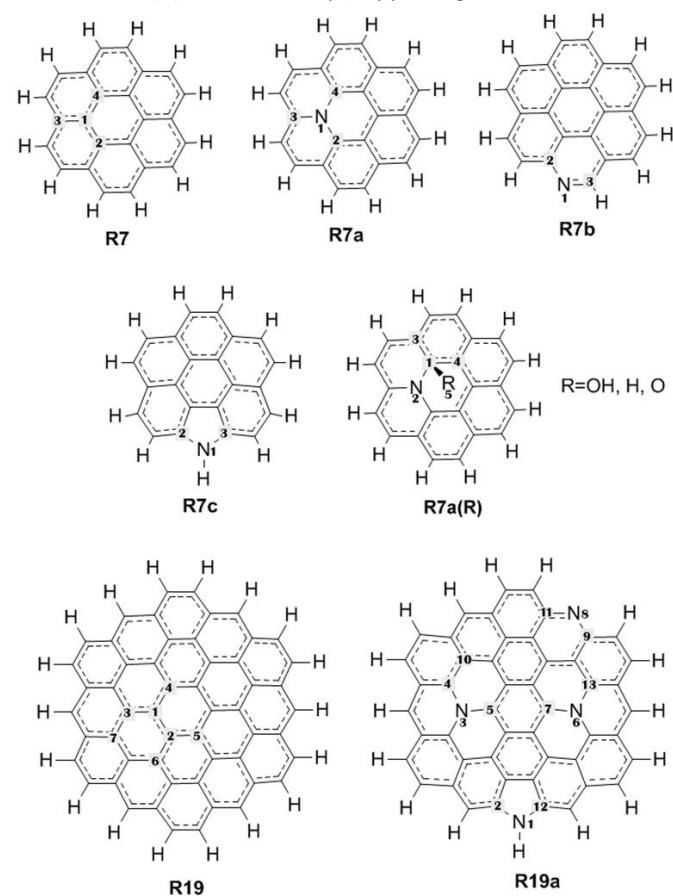

Figure 2 Model structures used to test the performance of PM6 for geometry optimizations.

1S to 4S). The mean unsigned error (MUE) in the distances are 0.016, 0.015 and 0.016 Å for R7, R19, and the whole set of distances, respectively, while for the angles the MUE are 1.36°, 0.81°, and 1.04°. Therefore, it can be stated that the deviations in geometry are similar regardless of the size of the cluster model used to mimic graphene. Moreover, they are also similar for pristine, as well as for N doped structures. In all the cases the percent deviation is lower than 1.2%. Considering the gathered geometrical data altogether the percent deviation between PM6 and PBE0/6-31+G(d) geometries is equal to 1.07%. This means that PM6 geometries are close enough to those of PBE0/6-31+G(d), and thus the B//A dual level strategy, which involves performing geometries optimizations with PM6 and then calculate energies using PBE0/6-31+G(d) at PM6 geometries is adequate. This strategy enables using a larger cluster model, with 37 rings, for the rest of the study.

In order to compare our results using clusters models, we have performed first-principles DFT spin-polarized calculations using the Perdew-Burke-Ernzerhof (PBE) exchange-correlation functional and the projector-augmented wave method as implemented in VASP 5.3.5 code. A Gamma centered 24X24X1 k-point mesh was used for sampling the Brillouin zone with an energy cutoff of 600 eV. These settings guarantee convergence of total energy differences within 0.01 eV. Our N-GN model contains 1 N and 31 C atoms. The positions of the atoms were fully relaxed in a hexagonal cell of a=9.85 and c=20.00 Å. A comparison between the density of states obtained for a N-GN graphitic cluster model, and the density of states of a N-GN graphitic periodic model is included in the supporting information (Fig. 7S). As observed, the density of states for the cluster model exhibits similar features to the ones displayed in the periodic calculation, suggesting that the proposed cluster models are able to capture the same chemistry of larger systems. Note that in both cases an increase of states near the Fermi level is observed.

Results and discussion

Experimental insights of the N-GN

After the rapid heating process, the obtained N-GN clearly shows voile-like structures with large voids and expansions between the graphene sheets (Fig. 3a). The highly opened structure of N-GN is attributed to the rapid heating process where the gases generated during the conversion expands the empty spaces between the sheets as they escape with very high kinetic energies. The morphology of N-GN is very different from previous reports of similarly thermally produced graphene that show accordion or work-like morphologies.[57, 58] In addition to the opened structure, the graphene sheets of N-GN are observed to have wrinkles, which likely have formed by the heterogeneous nitrogen atoms creating deformations in pristine graphitic structures due to exposure to ammonia during the heat treatment.[59] The wrinkled graphene sheets can also help to prevent re-stacking of N-GN to maintain active surface area which is crucial for the ORR activity. Similar to the SEM observations, the TEM image of N-GN shows folds and wrinkles
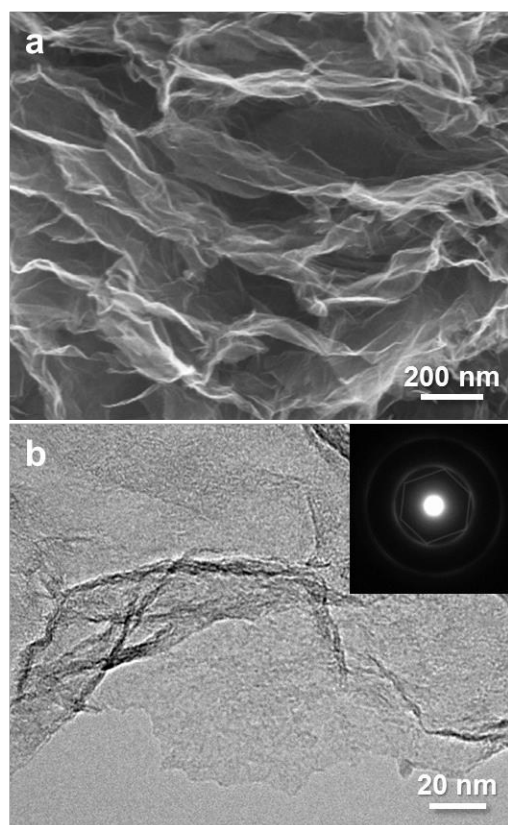

Figure 3 a) SEM, and b) TEM images of N-GN produced by rapid thermal treatment. Inset: SAED pattern of a few layers of N-GN. Reproduced with permission from J. Electrochem. Soc., 160, F910 (2013). Copyright 2013, The Electrochemical Society.

in the graphene sheets (Fig. 3b). The uneven edge of N-GN is another indication of the addition of nitrogen species, which have likely doped the edge of the graphene sheets more readily than the basal plane. In fact, the basal plane of N-GN is observed to still maintain its graphitic structure showing no large defects or perforations, which is very important for efficient transport of charges during the ORR. The selected area electron diffraction (SAED) pattern of the basal plane of N-GN shows a hexagonal symmetry, which signifies the existence of symmetrical three-fold sp² bonding of carbon atoms, again emphasizing primarily graphitic structure of N-GN.[60]

Of particular interest for the present study is the chemical characterization of the N-GN structures to evaluate their composition (i.e. nitrogen functional groups) and ORR mechanism. To this concern, X-ray diffraction was utilized to evaluate the structural change from GO to the N-GN after the synthesis carried out at 1100 °C using a rapid heating ramp. Fig. 4 shows a shift in the 002 reflection assigned to the layer-to-layer distance in the graphitic structures, as a result of the elimination of the oxygen groups of GO upon thermal reduction. As reported by McAllister et al,[57] the GO lowered down from a d-spacing of 8.57 Å (2θ =10.3°) to a value of 3.50 Å (2θ = 25.4°) for N-GN .
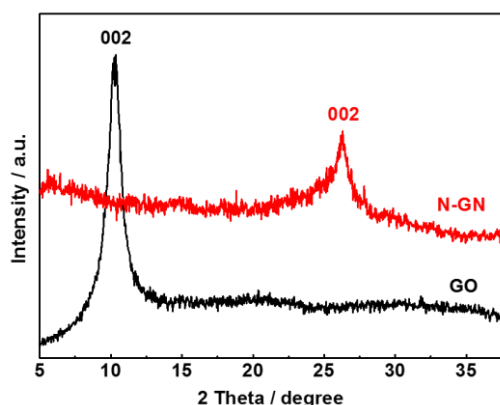
Figure 4 X-ray diffraction patterns collected for GO and N-GN samples. Reproduced with permission from J. Electrochem. Soc., 160, F910 (2013). Copyright 2013, The Electrochemical Society.

In order to confirm successful formation of N-GN through the structural deformation induced by thermal reduction and ammonia treatment, Raman spectra were collected for the GO and the N-GN. Fig. 5 shows two characteristic peaks obtained for both samples around 1350 (D band) and 1590 cm^{-1} (G band). The peak recorded at low shifts can be associated with some degree of disordering within the N-GN, triggered by defects in the planes. On the other hand, the peak located at high shifts is typical of the sp2 bonds with E2g vibrational mode, which are characteristic of any carbonaceous structure. In order to rationalize the intensity values of these bands in terms of the structural deformation, it is needed to calculate the ID/IG ratio. A comparison of these values reveal that a higher ratio of 1.14 is obtained for the N-GN, while 0.97 is estimated for the GO. Similar ratios have been reported in the literature.[61] This finding enables to confirm the expansion of GN and the incorporation of the heterogeneous nitrogen species into the graphitic structure, leading to the formation of N-GN structures having increased edge planes and favourable defects for electrocatalysis of ORR.
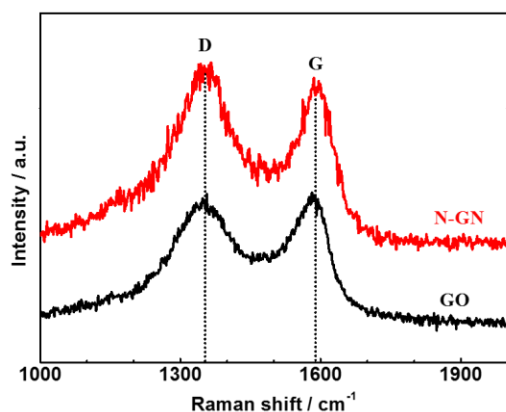

Figure 5 Raman spectra collected for GO and N-GN samples. Reproduced with permission from J. Electrochem. Soc., 160, F910 (2013). Copyright 2013, The

X-ray photoelectron spectroscopy was carried out to determine the N-bonding type contained in the N-GN. As observed in Figure 6a, the XPS spectra measured for the GO and N-GN structures display the typical peaks associated with the O and C species. The intense O peak results in the GO from oxygen groups formed during the implementation of Hummers' method, while its intensity decreases for N-GN as a result of the thermal reduction, which shrinks the oxygen content in the catalyst. A particular peak corresponding to the presence of nitrogen species is only detected for N-GN around 400 eV. Note that this peak is absent in the GO, thus, corroborating effective doping of nitrogen species in-plane the graphene nanosheets. Spectral de-convolution of nitrogen functional groups was carried out from the overall XPS spectrum measured for N-GN (Fig. 6a). Fig. 6b shows a high-resolution N1s spectrum of N-GN sample with a 3.5 at% of nitrogen distributed into three species: 1.59 at% pyridinic (45.4 %), 0.69 at% pyrrolic (19.6 %), and 1.22 at% graphitic (35 %), thus, confirming the existence of these nitrogen species at doping levels within the electrocatalyst. Electrochemical measurements were performed with the N-GN and commercial carbon supported 20 wt% Pt (Pt/C) catalysts to

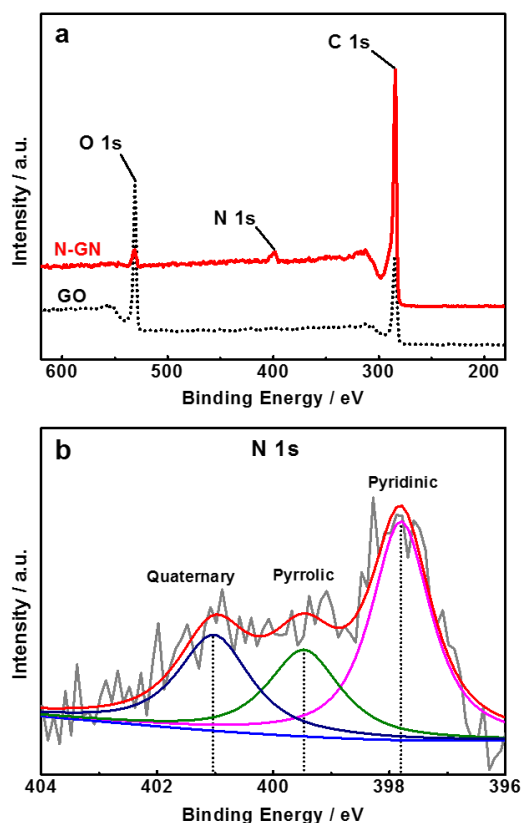**Figure 6** a) Full X-ray photoelectron spectroscopy spectra collected for GO and N-GN samples; b) De-convolution of nitrogen functional groups (N 1s) obtained from the overall XPS spectrum for N-GN. Gray line: original signal, red curve: curve fitting, blue: graphitic-type, green: pyrrolic-type, pink: pyridinic-type. Reproduced with permission from J. Electrochem. Soc., 160, F910 (2013). Copyright 2013, The Electrochemical Society.

ARTICLE

Journal Name

compare their ORR activity, and demonstrate their practical feasibility in O_2-saturated KOH electrolytes (0.1 M). Polarization curves were recorded for these materials from 0.2 V to -1 V using a scan rate of 10 mV s^{-1} and an electrode rotation speed of 900 rpm. All the electrochemical measurements were corrected from ohmic drop, by subtracting the currents obtained under the same testing conditions in an electrolyte previously bubbled with Argon gas.

The RDE measurements have been conducted with N-GN to obtain ORR polarization curves at various electrode rotation rates (Fig. 7a). Based on these curves, Koutechy-Levich (K-L) plot of N-GN has been obtained at various potentials -0.50, -0.55, and -0.60 V vs. SCE (Fig. 7b). The K-L analysis has been carried using the following equations.

$$\frac{1}{j} = \frac{1}{j_K} + \frac{1}{j_L} \qquad (1)$$

$$j_L = 0.2nFD_o^{2/3}v^{-1/6}C_o\omega^{1/2} \qquad (2)$$

The equation (1) shows relationship between the observed current density (j), kinetics current density (j_k), and limiting current density (j_L). Then the number of electrons transferred per O_2 molecule during the ORR, n, can be calculated using the K-L equation (equation 2), where F is the Faraday constant (96

485 C mol^{-1}), D_o is the diffusion coefficient of O_2 (1.9 x 10^{-5} cm^2 s^{-1}) in 0.1 M KOH, v is the kinematic viscosity of 0.1 M KOH (0.01 cm^2 s^{-1}), and C_o is the concentration of O_2 in the electrolyte (1.1 x 10^{-6} mol cm^{-3}).[62] At the ORR potentials of -0.50 V, -0.55 V, and -0.60 V vs. SCE, the calculated value of n is 4.0, which is an indication of highly efficient electrochemical reduction of O_2 occurring via a pseudo four-electron reduction pathway (O_2 + $2H_2O$ + 4e$^-$ → 4OH$^-$). Typically, ORR using a metal-free carbon-based catalyst involves an electron number less than four. However, highly ORR active nitrogen-doped carbon species have been reported in the literature to undergo the four-electron pathway.[33, 63]

Fig. 8 shows the ORR curves of N-GN and commercial Pt/C catalysts obtained at 900 rpm, which are shown to demonstrate comparable on-set potentials of -0.050 and -0.039 V vs. SCE, respectively. In terms of half-wave potential, N-GN outperforms commercial Pt/C by demonstrating -0.164 V vs. SCE compared to more negative shifted potential of -0.179 V vs. SCE obtained with Pt/C. Additionally, both N-GN and Pt/C demonstrate comparable limiting current densities at the high overpotential region. These results are indicative of excellent ORR activity of N-GN as a metal-free carbon-based catalyst.

To date, the remarkable ORR performance on nitrogen doped graphene nanosheets has been established, however, the specific electroactive nitrogen species towards ORR could not be determined using the above experimental results. It is only clear that the overall nitrogen content influences the ORR electrocatalysis, but this may not be the most crucial factor as a specific nitrogen species can be more effective towards improving ORR. This is in line with the finding that not all nitrogenated carbon materials catalyse the ORR.[64] Table 1 and other studies in the literature show a general trend for N-doped carbonaceous materials, when the growth temperature is increased, the nitrogen content within the catalysts decreases due to the decomposition of the nitrogen species at high temperatures.[25, 52, 59, 65] Likewise, the nitrogen type varies with the augment of the synthesis temperature. Graphitic N is typically more predominant at high temperatures above 750 °C, while pyridinic N is more abundant in catalysts formed below
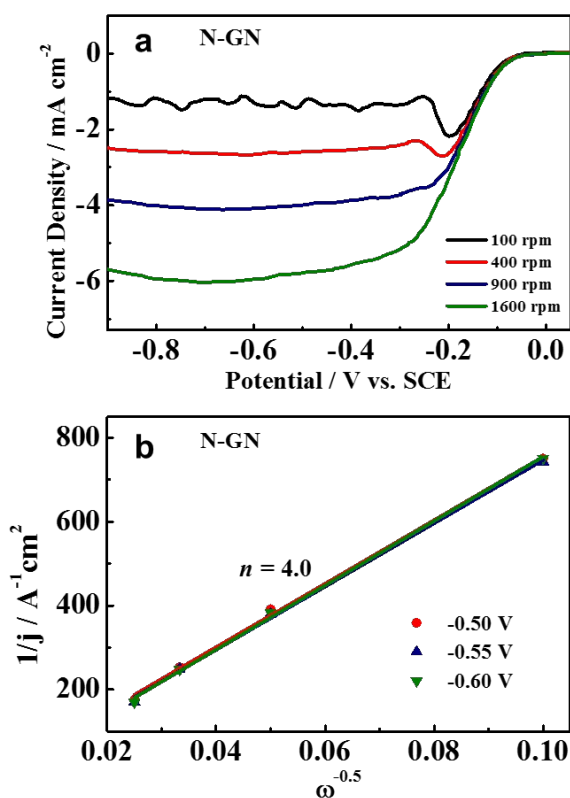

Figure 7 a) RDE measurements of N-GN obtained at rotation rates of 100, 400, 900, and 1600 rpm; b) Koutechy-Levich plot of N-GN obtained at potentials -0.50, -0.55, and -0.60 V vs. SCE. Reproduced with permission from J. Electrochem. Soc., 160, F910 (2013). Copyright 2013, The Electrochemical Society.
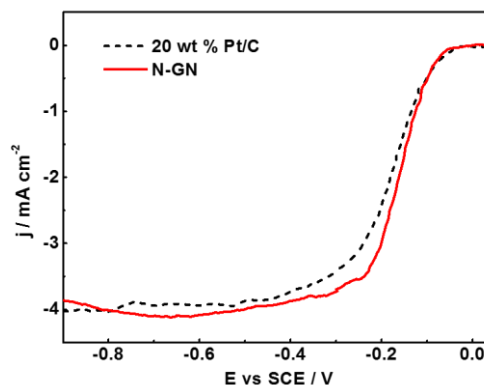

Figure 8 ORR polarization curves of Pt/C and N-GN obtained at 900 rpm. Reproduced with permission from J. Electrochem. Soc., 160, F910 (2013). Copyright 2013, The Electrochemical Society.

550 °C, although this condition may depend on the precursor.[24, 25, 67, 68] Nevertheless, electrochemical characterization of ORR should be connected to these compositions in order to determine more electroactive sites for this reaction. This conclusion is difficult to draw from the composition of nitrogen species reported in the literature for different N -doped carbonaceous materials (Table 1), as a result of the multiple conditions (e.g. precursor, temperature, substrate, time, technique) of synthesis utilized to prepare the materials. Although most studies have assigned the ORR electrocatalysis

to graphitic N and pyridinic N (in that order, refer to Table 1). These particular asseverations only rely on the individual at% of the nitrogen species found from XPS analysis, or a higher at% increase compared when a determined variable is being modified during synthesis (e.g. temperature, precursor), thus, there is a divided opinion. A fairer comparison can be established by analysing the single reactivity of each nitrogen species and their adjacent carbons, considering the presence of all nitrogen species which have been experimentally confirmed

Table 1 Distribution of Nitrogen species calculated from the de-convolution of the N 1s peaks of XPS analysis obtained from different sources in the literature.

Carbonaceous structure	Temp. * (°C)	Total N content (at %)	Nitrogen species pyridinic N (at %)	pyrrolic N (at %)	graphitic N (at %)	Oxidized N (at %)	Ref.
N-Graphene	300-1100	~ 3-5	Not quantified — Higher temperature (≥ 900 °C) incorporated more graphitic N into the graphene				2,65
1-NG	800	5	(33 %)	(26 %)	(15 %)	(25 %)	20
2-NG		3	(42 %)	(26 %)	(24 %)	(8 %)	
3-NG		5	(45 %)	(29 %)	(21 %)	(5 %)	
1-NC	800	6	(56 %)	(24 %)	(12 %)	(8 %)	21
2-NC		4	(50 %)	(26 %)	(15 %)	(9 %)	
N-CNT-DCDA	800	3.7	(59 %)	(25 %)	(16 %)	-	22
N-CNT-CM		2.3	(54 %)	(33 %)	(13 %)	-	
N-CNT ** ED		4.74	1.6633 (35.09 %)	2.1761 (45.91 %)		0.9006 (19 %)	
N-CNT ** DAP	800	2.48	0.3678 (14.83 %)	1.6916 (68.21 %)		0.4206 (16.96 %)	26
N-CNT ** DAB		1.20	0.3492 (29.10 %)	0.7604 (63.37 %)		0.0904 (7.53 %)	
N-CNT ** P4VP		4.3	1.7 (39.53 %)	0.4 (9.30 %)	2.2 (51.17 %)	-	
N-CNT ** PMVI	1173	8.4	5.2 (61.90 %) ***	0.4 (4.76 %)	2.8 (33.34 %)	-	27
N-CNT ** P4VP		10.7	4.3 (40.19 %)	0.7 (6.54 %)	5.7 (53.27 %)	-	
N-Graphene	900	-	Not quantified — Larger amount of graphitic N presents a higher ORR electrocatalysis than pyridinic N				50
N-Graphene	800	2.8	1.5455 (55.20 %)	0.9352 (33.40 %)	0.3192 (11.40 %)	-	59
N-Graphene	900	2.8	1.5596 (55.76 %)	0.8484 (30.33 %)	0.3892 (13.91 %) ***	-	
N-Porous Carbon		6.88	1.85 (26.89 %)	1.69 (24.56 %)	2.06 (29.94 %)	1.28 (18.61 %)****	66
N-Porous Carbon	1000	3.51	0.96 (27.35 %)	-	1.49 (42.45 %)	1.06 (30.2%)****	
N-Porous Carbon		3.47	0.68 (19.59 %)***	-	2.26 (65.13 %)***	0.53 (15.28%)****	

* Synthesis condition

** Modification of the precursor

*** Highest ORR electrocatalysis assigned to a specific N species in the study

**** Pyridinic N^+-O^-

ARTICLE

Journal Name

(Figure 6). This approach cannot be evaluated experimentally, whence ab initio methods for these purposes.

DFT analysis

The cluster models used to mimic pristine and N doped graphene nanosheets are shown in Fig. 9, and were constructed based on the structures experimentally synthesized and characterized (refer to the previous section). For the N-GN we have included structures with increasing number and varying proportions of the different N sites (graphitic, pyridinic, and pyrrolic) to help analysing the effects of these sites on the graphene reactivity.

Since the oxygen reduction is the key factor studied in this work, the oxidation of N modified graphene was first

investigated. To that purpose vertical ionization energies (VIE) have been calculated as:

$$VIE = E_{N-1}(g_N) - E_N(g_N) \qquad (3)$$

where $E_N(g_N)$ and $E_{N-1}(g_N)$ are the total energies of the N and $(N-1)$-electron systems calculated at the g_N geometries. In addition the band gap (BG), considered as the energy difference between the highest occupied molecular orbital (HOMO) and the lowest unoccupied molecular orbital (LUMO) has also been analysed. These two criteria (VIE and BG) are expected to be inversely proportional to the facility of the electron transfer through the studied materials.

Due to the inherent structure of the different N sites, in the calculations their presence have an effect on the multiplicity of
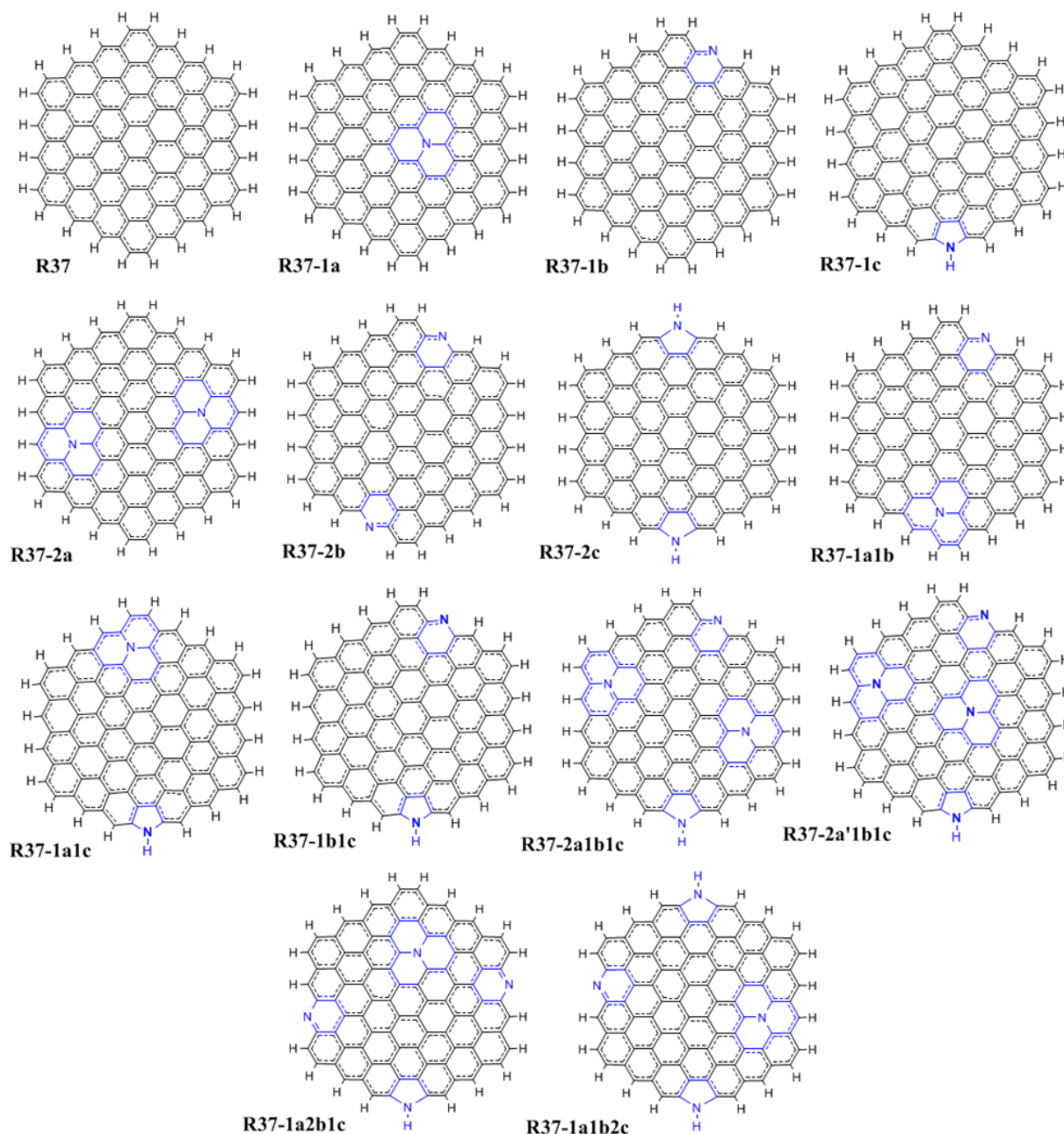

Figure 9 Model structures used to mimic pristine and N doped graphene

the whole system, depending on the number of graphitic N sites (type a). The structures with an odd number of this kind of sites are open shell systems, and thus their IE and BG are expected to be lowered by this reason. Thus, the results obtained in these cases should be analysed carefully. This is also why we have included several structures with even number of graphitic sites, i.e. to guarantee that the comparisons with other structures allow drawing fair conclusions about the relative effects of the different sites. Another important consideration is that because pyridinic (b) and pyrrolic (c) sites are, necessarily, terminal sites; they will be less abundant than graphitic sites in experimentally produced materials, unless the catalysts contain a considerable amount of defects. For the structure with 4 N sites, two of them being graphitic N, we have used two different models, one with both sites near the edge of the structure (R37-2a1b1c) and the other one with one graphitic site close to the center of the structure (R37-2a'1b1c) to investigate the possible influence of location on the effects from this type of sites.

The first finding that stands out is that the presence of the N sites systematically reduces the BG of the modeled structures (Table 2) regardless of the type or number of N. This strongly suggests that the electron flux through the N doped structures is increased with respect to the pure C. As mentioned before the models that are open shell species (indicated with a * in Table 2) present significantly lower BG values than the pristine C structure. However, this is caused at least in part for presence of an unpaired electron. These models are included in the present study only for possible further theoretical studies in the subject. Among the closed shell species R37-2a presents the lowest BG value, followed by R37-2a'1b1c then R37-2a1b1c. All the other studied closed shell species have BG values, which are only slightly lower than that of the pure C structure. It seems interesting to note that such structures do not present graphitic N sites. In addition comparing the values for R37-2a'1b1c and

R37-2a1b1c it seems that the effect of increasing the electron flux, caused by the presence of graphitic N sites is larger when these sites are located in central positions, instead of near the edges. This seems to be an important finding since, as mentioned before, central graphitic sites are expected to be the most abundant sites in actual doped materials, due to the proportions of central vs. terminal sites in N-GN structures.

Regarding VIE, the effect of the N sites is also to reduce their values. However, in this case three exceptions were found. They correspond to structures R37-1b, R37-2b, and R37-1b1c, with the highest value of VIE corresponding to R37-2b. It is interesting to note that these structures are just the ones that do not present graphitic N sites. On the other hand the lowest VIE value corresponds to structure R37-2a, which also presents the lowest BG value, among all the studied closed shell species. These results suggest that the presence of graphitic sites in carbon surfaces might be crucial to increase their catalytic properties, since they seem to be related with the decreasing of ionization energies, i.e. the materials presenting this type of sites are more easily oxidable.

The next step in the investigation deals with the interaction of the studied structures with several chemical species that are expected to be present in the actual systems ($^3O_2$, $^\bullet OOH$, ^3O, $^\bullet OH$, and $H^\bullet$). To that purpose we have used only the R37-2a'1b1c structure because it includes all types of the N sites, is a closed shell structure, and presents graphitic N sites in two different relative positions, i.e. near the center and the edge. The site numbering referred in the present study regarding the adsorption of the chemical species mentioned above is shown in Fig. 10. It has been established in such a way that the starting letter indicates the type of N site, i.e. a for graphitic (central), a' for graphitic (close to the edge), b for pyridinic, and c for pyrrolic. For comparison, similar calculations of the interactions

Table 2 Vertical ionization energies (VIE, eV), and HOMO-LUMO band gaps (BG, eV) for the computed structures.

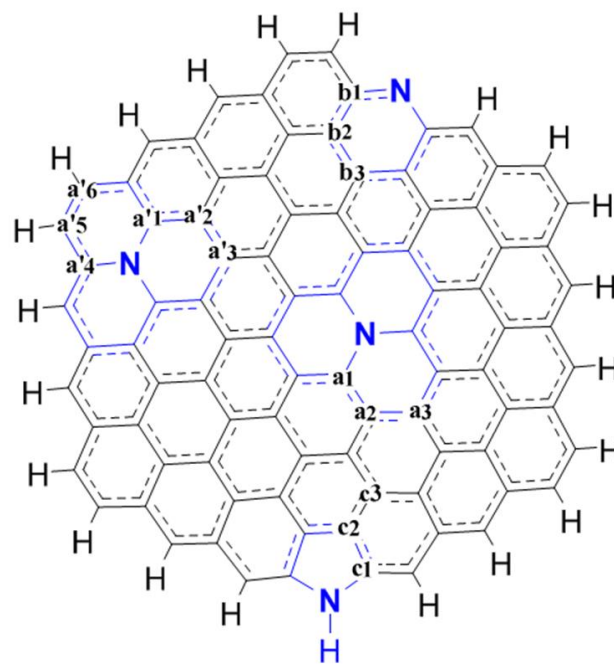| Structure	N site	Multiplicity	VIE	BG
R37	0	1	5.88	2.47
R37-1a *	1	2	4.47	1.04
R37-1b	1	1	5.95	2.39
R37-1c	1	1	5.87	2.43
R37-2a	2	1	4.36	0.86
R37-2b	2	1	6.03	2.32
R37-2c	2	1	5.75	2.39
R37-1a1b *	2	2	4.65	0.96
R37-1a1c *	2	2	4.57	1.05
R37-1b1c	2	1	5.90	2.39
R37-2a1b1c	4	1	4.56	1.12
R37-2a'1b1c	4	1	4.59	0.97
R37-1a2b1c *	4	2	4.76	0.92
R37-1a1b2c *	4	2	4.63	1.17

* Open shell structures.

Figure 10 Site numbering in the R37-2a'1b1c to account for the adsorption processes.

ARTICLE

Table 3 Bond distances (Å) for the adsorption of the intermediates participating in the ORR mechanism.

	$\cdot OOH$	^3O	$\cdot OH$	$\cdot H$
Pristine G	1.500	1.411	1.452	1.148
a1	1.489	1.235	1.446	1.141
a2	1.485	1.476 1.459	1.449	1.144
a3	1.486	1.401	1.451	1.141
a'1	1.478	1.408	1.439	1.142
a'2	1.498	1.377	1.455	1.148
a'3	1.491	1.474 1.474	1.453	1.143
a'4	1.474	1.379	1.441	1.141
a'5	1.453	1.358	1.439	1.120
a'6	1.460	1.401	1.436	1.118
b1	1.459	1.254	1.444	1.129
b2	1.460	1.372	1.430	1.126
c1	1.484	1.470 1.468	1.448	1.147
c2	1.490	1.284	1.452	1.143
c3	1.495	1.283	1.455	1.148

Table 4 Gibbs free energies (ΔG, kcal mol^{-1}) for all possible adsorption processes (refer to Fig. 10) occurring on pristine graphene and N-GN.

	$^3O_2$	$\cdot OOH$	^3O	$\cdot OH$	$\cdot H$
Pristine G	-5.61	12.61	-7.76	-9.60	-17.12
a1	-8.81	-23.77	-55.20	-48.26	-44.58
a2	-7.59	-8.77	-53.23	-31.83	-27.27
a3	40.45	-17.99	-33.24	-40.85	-42.31
a'1	16.12	-21.12	-47.36	-44.11	-43.75
a'2	-6.95	-0.64	-28.08	-24.07	-18.69
a'3	-6.66	-16.17	-43.99	-37.07	-39.32
a'4	0.89	-9.08	-45.14	-33.24	-27.80
a'5	27.45	0.28	-30.76	-27.57	-38.13
a'6	4.87	-15.18	-44.00	-34.71	-43.76
b1	-1.72	1.65	-41.17	-27.31	-25.51
b2	16.47	-8.98	-35.28	-30.01	-36.30
c1	-7.72	4.93	-35.08	-17.88	-18.25
c2	-7.04	-0.21	-24.98	-23.15	-26.53
c3	4.76	-0.49	-16.61	-23.62	-15.36

of the $^3O_2$, $\cdot OOH$, ^3O, $\cdot OH$ and $\cdot H$ species in the site a1 of an un-doped pristine graphene structure are carried out.

For the direct $^3O_2$ adsorption on the different sites, any attempt to bond one of the O atoms to the sheet invariably led to the separation of the fragments, i.e. no chemical adsorption was found on any of the studied sites. When the modelling is performed trying to obtain a double anchored structure, i.e. with both O atoms bonded to the surface the reactions become thermochemically unviable, with significantly positive Gibbs energies of reaction. Therefore, these results indicated that the oxygen does not bind to the studied non-doped and doped surfaces, and in the last case regardless of the presence of different N sites.

For all the other cases ($\cdot OOH$, ^3O, $\cdot OH$, and $\cdot H$) proper adsorption products were found at all the studied sites. The bond distance of the formed adducts are reported in Table 3. In general for the formed O-C bonds the distances increase in the following order ^3O, $\cdot OH$, $\cdot OOH$. In the particular case of ^3O the formation of an epoxy-like structure was found for the adsorptions on sites a2, a'3 and c1, resulting in two values of the formed bond distances for these cases as reported in Table 3. For all the other sites the adsorption lead to the formation of one C-O bond at the intended site.

The Gibbs free energies for all the studied reaction channels (ΔG) are reported in Table 4. T*ΔS and ΔZPE values calculated for the adsorption processes occurring on pristine graphene, and the a1 site on N-GN are reported in Table 5S (Supporting Information). For ^3O, $\cdot OH$, and H$\cdot$ all the addition reactions were found to be exergonic. This indicates that these species have high reactivity, and low site selectivity towards the studied structures. On the other hand, for $\cdot OOH$ −that is relatively less reactive− the adsorption process was found to be endergonic

when taking place on sites a'5, b1 and c1. In addition the adsorption on sites a'2, c2 and c3 are predicted to be almost isoergonic. At all the other sites the $\cdot OOH$ adsorption processes were found to be exergonic. Note that the Gibbs free energies for the $^3O_2$ adsorption are in general more positive (i.e. endergonic) than the adsorption of any other species ($\cdot OOH$, ^3O, $\cdot OH$, and $\cdot H$) on any site on N-GN. Similarly as occurs for $\cdot OOH$, the $^3O_2$ adsorption are both exergonic and endergonic. The more abundance of endergonic adsorption sites (a3, a'1, a'4, a'5, a'6, b2 and c3) on N-GN would account for the electrolysis demanded in the ORR process.

Compared to the pristine C surface, the N doping systematically increases the thermochemical viability of the $\cdot OOH$ and ^3O adsorptions. For the H adsorption this trend is also fulfilled with the exception of the reaction involving the c3 site. For the $\cdot OH$ absorption, on the contrary, only those taking place on sites a1, a3, a'1, a'3, and a'6 have ΔG values more negative than that of the pristine C surface. In addition, the most negative ΔG values are systematically those involving sites a1 and a'1. These findings suggest that the presence of graphitic N sites is the most important one to increase the viability of the adsorption of the studied species ($^3O_2$, $\cdot OOH$, ^3O, $\cdot OH$, and $\cdot H$). This seems to be the case regardless of the location of this kind of sites, whether central or near the edge.

In order to improve our energy predictions, further calculations were performed using the implicit solvent (water) on the site a1 (refer to Table 5), which in the previous section was found to present the most negative ΔG value among all possible sites considered on the catalyst computed in gas phase. As observed in this table, the trends observed for the ΔG values calculated in gas phase are consistent to those obtained with the implicit solvent, namely the ΔG for the $^3O_2$ adsorption are in

general more positive than the adsorption of any other species on N-GN, and the most positive ΔG is obtained for the OOH on the pristine graphene. Presumably, this finding confirms that the first elementary steps of the ORR mechanism involving $^3O_2$ and OOH species play a role as rate-determining step. In addition, a comparison of the ΔG values reported in Table 5 for the pristine and N-GN samples shows that the adsorption of all species on N-GN is considerably more exergonic than on pristine graphene, demonstrating its better capacity to perform the ORR on its surface. In addition, the ΔG values becomes more negative using implicit solvent (H_2O), which agrees with the results reported by Yu et al.[30] T*ΔS and ΔZPE values calculated for the adsorption processes occurring on pristine graphene, and the a1 site on N-GN using the implicit solvent model are reported in Table 6S (Supporting Information).

Calculation of reversible potentials on the basis of Gibbs energies

The ORR mechanism under alkaline conditions has been moderately reported and analysed in the literature,[30] unlike the ORR mechanism occurring under acidic conditions. The elementary steps of the associative mechanism for the ORR are described in Table 7. Electroactive species are written in bold, * denotes a free active site on the electrode surface. The standard reduction potentials Uᵒ (V/ SHE) of reactions (2-5) are evaluated using Hess's law and the standard reduction potentials from the elementary steps of the ORR mechanism in acid media.[31] The associative mechanism is the most common pathway (i.e. more energetically favourable) reported for the ORR under alkaline conditions,[30] whence these reactions will be the motivation of the present analysis. It differs with the dissociative mechanism in the first three steps (reactions 1-3), which are replaced by $\frac{1}{2}O_2 + * \rightarrow O_{ads}$, and then followed similarly by reactions (4) and (5). The Uᵒ value of reaction step (3) could not be calculated since equivalent information under acidic conditions was not found. However, as described below this does not affect the calculation of the surface electrode potential of other reactions, but precludes calculating a free energy diagram which requires the consecutive addition of the free energy of each elementary reaction step.

The research groups of Anderson and Nørskov have proposed similar comprehensive theories to calculate the potential of multiple electrochemical reactions, particularly the ORR mechanism in acidic conditions on a Pt surface. The formalisms and developments of these models are not herein presented, but only their fundamental considerations. Further details of these models can be consulted in the literature.[31, 33, 69-75]

The linear Gibbs energy relationship (LGER) developed by Anderson and colleagues calculates the reversible potential of an electrochemical reaction involving adsorbed (i.e. chemisorbed) or soluble (i.e. physisorbed) reactant/products on the electrode surface, by considering that the reversible potential of the reaction is made up from two inputs: the standard reduction potential (U°) of the electrochemical reaction estimated under standard conditions against the standard hydrogen electrode (SHE), and the Gibbs free energies involving the adsorption of all products and reactants of the reaction (ΔG). The core of this method is that the electrode surface potential of adsorbed species can be estimated as a perturbation of the reversible potential of the same species but participating in a redox reaction (i.e. solution bulk), since they are bonded to the surface. This model can account for the ORR mechanism since there is a linear behaviour established between gas phase reaction energies and the standard reversible potentials of the reactions of this mechanism. It relies on some assumptions described in refs.[69, 70] In this model, the bond strength (Bond_s) between the adsorbate and the electrocatalyst surface (i.e. N-GN) can be estimated using the following equation:[33]

$$Bond\_s = G_{N-GN} + G_{adsorbate} - G_{adsorbate\_N-GN} \qquad (4)$$

where G_{N-GN}, $G_{adsorbate}$, $G_{adsorbate\_N-GN}$ are the Gibbs free energies in eV of the N-GN structure, the adsorbate (i.e. $^3O_2$, ·OOH, ^3O, ·OH, ·H) and the adsorbate species on N-GN, respectively. The model assumes that the solvation interactions arising in all the species involved in the charge transfer reaction are equally decreased since the intermediates are bonded to the surface. Therefore, the adsorption bond strengths calculated with eq. (4) (Table 6) can be used to estimate the reversible potential of the surface intermediates participating in the ORR:[33]

$$U_{surface} = U° + \frac{Bond\_s_{product} - Bond\_s_{reactant}}{nF} \qquad (5)$$

where $Bond\_s_{product}$ and $Bond\_s_{reactant}$ are the product and reactant adsorption bond strenghts, respectively, n is the number of electrons transferred in the electrochemical reaction and F is the Faraday constant (96485.5 C mol⁻¹).

On the other hand, the method established by Nørskov and colleagues also estimates the free energies of all intermediates participating in the ORR, as a function of the electrode potential obtained from adsorption energies computed for the intermediates using DFT.[71-75] The model has been successfully utilized to estimate thermodynamically the cathode reactions of the ORR on different metals, and is able to predict a volcano-shaped relationship between the rate of the reactions and the

Table 5 Gibbs free energies (ΔG, kcal mol⁻¹) for the adsorption processes occurring on the a1 site (refer to Fig. 10) on pristine graphene and N-GN using implicit solvent.

	$^3O_2$	·OOH	^3O	·OH	·H
Pristine G	-5.95	13.52	-20.67	-9.18	-19.36
a1	-9.53	-23.07	-66.27	-47.99	-47.62

Table 6 Bond strengths (Bond_s, eV) for the adsorption processes occurring on the a1 site (refer to Fig. 10) on N-GN using gas and implicit solvent phases.

	$^3O_2$	·OOH	^3O	·OH	·H
Gas phase	0.382	1.031	2.394	2.093	1.933
Implicit solvent	0.413	1.000	2.874	2.081	2.065

ARTICLE   Journal Name

Table 7 Standard (U^o) and theoretical surface ($U_{surface}$) potentials calculated for the elementary steps of the ORR mechanism occurring in alkaline conditions. The $U_{surface}$ values were calculated using U^o and the Gibbs free energies for the adsorption processes occurring on the a1 site (refer to Fig. 10) on N-GN structures, using density functional methods in gas and implicit solvent models.

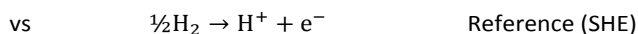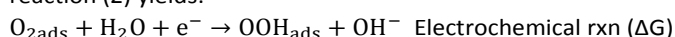| Elementary reduction reactions		$U^{o\dagger}$ (V/SHE)	$U_{surface}^{gas}$ (V/SHE)	$U_{surface}^{H_2O}$ (V/SHE)
$O_2 + * \rightarrow O_{2ads}$	(1)			
$O_{2ads} + H_2O + e^- \rightarrow OOH_{ads} + OH^-$	(2)	-0.874	-0.226	-0.287
$OOH_{ads} + e^- \rightarrow O_{ads} + OH^-$ ‡	(3)	‡	‡	‡
$O_{ads} + H_2O + e^- \rightarrow OH_{ads} + OH^-$	(4)	1.219	0.918	0.426
$OH_{ads} + e^- \rightarrow OH^- + *$	(5)	1.980	-0.112	-0.101

† This study

‡ It could not be determined

oxygen adsorption energy. The formalism of the model establishes that an electrochemical reaction referred to the standard hydrogen electrode (SHE, reference) can be rewritten only in terms of a redox reaction, since the free energy of the electron in the electrochemical step is a difficult concept to evaluate. Thus, the reaction free energy of each step of the ORR adapted to the present case study occurring under alkaline conditions can be computed as follows:[71-75]

$$\Delta G = \Delta G^0 + \Delta G_w + \Delta G_U + \Delta G_{field} + \Delta G_{pH} \quad (6)$$

Each term in equation (6) are described below.

Any electrochemical reaction is typically measured against the SHE. The reaction free energy of $\frac{1}{2}H_2 \leftrightarrow H^+ + e^-$ is zero at an electrode potential of U = 0 at T=298 K, pH =0 in the solution, 1 bar of H_2 in the gas phase. Under standard conditions, the Gibbs free energy $\Delta G_0 = \Delta G$ of the reaction $A_{ads} + H_2O + e^- \rightarrow AH_{ads} + OH^-$ (Electrochemical cathodic reaction) can be calculated as $A_{ads} + \frac{1}{2}H2 \rightarrow AH_{ads}$ (Redox reaction). A_{ads} and AH_{ads} correspond to the adsorbed reactant and product (i.e. gaining H) on the catalyst. The implementation of this procedure for reaction (2) yields:

$O_{2ads} + H_2O + e^- \rightarrow OOH_{ads} + OH^-$ Electrochemical rxn (ΔG)

vs $\frac{1}{2}H_2 \rightarrow H^+ + e^-$ Reference (SHE)

$O_{2ads} + \frac{1}{2}H_2 \rightarrow OOH_{ads}$ Redox reaction (ΔG_0)

- ΔG^0 calculations for the redox reactions were only obtained using theoretical information. Refer to computational details.
- Water was not explicitly considered as a monolayer on the surface of the N-GN, only implicitly, whence the term ΔG_w is neglected. This will be the motivation of a forthcoming study, since it involves molecular dynamics (MD).
- The effect of electron transfer is considered with the term ΔG_U = -eU°, where U° is the standard reduction potential of the electrochemical reaction, and e the number of electrons.
- Electrical double layer effects are neglected, $\Delta G_{field} \approx 0$.

- The correction for the free energy of H+ due to the concentration dependence of the entropy can be calculated using: ΔG_{pH} = kT ln(10*pH) = 2.89 kcal mol⁻¹ (pH = 13), where k is Boltzmann constant (8.617332478 ×10⁻⁵ eV K⁻¹).

In order to establish a fair comparison between the models proposed by Anderson and Nørskov research groups, ΔG_w, ΔG_{field} and ΔG_{pH} are not considered. Note that eq. (5) proposed by Anderson and colleagues only involves the first and third term of eq. (6) developed by Nørskov et al, e.g. $\Delta G_U = -eU^o$ and $U_{surface}$ = U° + (Bond_$s_{product}$-Bond_$s_{reactant}$)/nF. Thus, the electrode surface potential ($U_{surface}$) associated with the reduction of the adsorbed species (reactions 2-5) in alkaline media can be calculated either using eq. (5) or eq. (6) (e.g. neglecting ΔG_w, ΔG_{field}, ΔG_{pH}). These results are shown in Table 7.

As shown in this table, the $U_{surface}$ values determined in gas phase are more positive than using implicit solvent, except reaction (5). In general, this could be due to the fact that more energy is required to reduce an electroactive species in the presence of the solvent than in gas phase. Although the effects of the terms ΔG_w, ΔG_{field} and ΔG_{pH} in eq. (6) can become important under alkaline conditions, particularly the presence of explicit water in the calculations (i.e. refer to reactions 3 and 5), first insights of the surface electrode potential can be established between the comparison of the theoretical calculations shown in Table 7 and the value determined in alkaline conditions for a multi-step mechanism (i.e. two-electron transfer step)[76, 77]. This comparison reveals that the experimental transformation of OOH⁻/OH⁻ involving the last 2-electronic transfer steps (i.e. 4 electrons transferred in total) performed under standard conditions presents an electrode potential of 0.867 V. As observed in Table 6, the highest bond strength reported on N-GN (i.e. a1 site) occurs for the O adsorption, which suggests that the removal of this species to form OH_{ads} (reaction 4 in Table 7) on the electrode surface is the rate-controlling step of the ORR mechanism. This finding agrees with the analysis conducted by Yu et al.[30] on graphene doped only with graphitic N-type sites in alkaline conditions. Note that

this implies that the last electron transferred in reaction (5) will not represent a significant contribution to the energy barriers of the mechanism, whence its reduction potential will be virtually the same as the preceding rate-controlling step. A similar comparison has been established by Kurak and Anderson in acid media.[31] Under this premise, the electrode potential of 0.867 V[76, 77] can be compared with the 0.918 V calculated theoretically for reaction (4) (Table 7) in gas phase. This demonstrates a small deviation of 0.051 V against the two electronic transfer step forming OH^-. Note that the model is thermodynamically favourable to estimate the potential of the rate determining step in N-GN structures containing from 3.42 (R19a in fig. 2) to 5.8 (R37-2a'1b1c in fig. 9) at % N, calculating values of 0.856 and 0.918 V, respectively. These values are not so different if the nitrogen doping variation is considered. Likewise, the calculation of this potential for a bi-layer structure (not shown) 1.69 at % N (C187-H46-N4) turns out to be 0.893 V, which is similar to the value obtained for the cluster model analysed in most of the present work. A larger deviation is observed for the surface electrode potential calculated with the value obtained under conditions of implicit solvent, which requires a more profound analysis of the role of explicit water hydration on this electrode potential value.

Conclusions

This study evaluated the performance of the Oxygen Reduction Reaction on N-doped graphene nanosheets synthetized with a one-step method, relying on extremely rapid heating of graphene oxides from room temperature to higher temperatures than 800 °C within five seconds (temperature ramps $\geq$ 150 °C s^{-1}). Raman and X-ray photoelectron spectroscopy showed an efficient nitrogen incorporation into the graphitic network. The electrochemical testing conducted in alkaline media with a rotating disk electrode technique revealed that the N-doped graphene nanosheets presented a very comparable Oxygen Reduction Reaction electroactivity to the state-of-the-art commercial 20 wt% Pt/C catalyst, which was assigned to the highly opened structured attained with the synthesis method. Density functional theory was used to determine the bandgap, vertical ionization energies, and adsorption free energies of the intermediate species ($^{\bullet}OOH$, $3O$, $^{\bullet}OH$, and $^{\bullet}H$) formed on the nanosheets during the ORR associative mechanism occurring in alkaline media. It was determined that a larger cluster model with 37 rings doped with all nitrogen bonding (e.g. pyridinic, pyrrolic and graphitic) is needed to account for the properties of the catalyst. The adsorption on top of any carbon adjacent to a central graphitic nitrogen generated a significant reduction in the energy barrier of the ORR electrocatalysis, from all possible adsorption sites for the intermediates including nitrogen. The bond strengths between all possible species and the N-doped graphene showed that the removal of $3O$ species from the electrode surface to form OH_{ads} was the rate-controlling step of the ORR mechanism. The surface electrode potential of 0.918 V computed for this reaction step was close to the 0.867 V reported for the second

reaction (OOH^-/OH^-) of the mechanism with two consecutive 2-electron transfer steps obtained under standard conditions.

Further theoretical evaluations using explicitly water will be the motivation of a forthcoming study to determine the influence of water hydration on the energetics required to perform the ORR electrocatalysis on N-doped graphene nanosheets.

Acknowledgements

Notes and references

1. Z. Chen, M. Waje, W. Li and Y. Yan, *Angew. Chem. Int. Ed.* , 2007, **46**, 4060.
2. X. Wang, W. Li, Z. Chen, M. Waje and Y. Yan, *J. Power Sources*, 2006, **158**, 154.
3. N. Mano, V. Soukharev and A. Heller, *J. Phys. Chem. B*, 2006, **110**, 11180.
4. N. Alonso-Vante, H. Tributsch and O. Solorza-Feria, *Electrochim. Acta*, 1995, **40**, 567.
5. O. Solorza-Feria, K. Ellmer, M. Giersig and N. Alonso-Vante, *Electrochim. Acta*, 1647, **39**, 1994.
6. K. Gong, F. Du, Z. Xia, M. Duratock and L. Dai, *Science*, 2009, **323**, 760–764.
7. E. Biddinger, D. v. Deak and U. Ozkan, *Top. Catal.*, 2009, **52**, 1566-1574.
8. Junbo Hou, Yuyan Shao, Michael W. Ellis, Robert B. Moored and B. Yi, *Phys. Chem. Chem. Phys.*, 2011, **13**, 15384–15402.
9. G. Wang, J. Yang, J. Park, X. Gou, B. Wang, H. Liu and J. Yao, *J. Phys. Chem. C*, 2008, **112**, 8192–8195.
10. D. Yang, A. Velamakanni, G. Bozoklu, S. Park, M. Stoller, R. D. Piner, S. Stankovich, I. Junga, D. A. Field, C. A. Ventrice Jr. and R. S. Ruoff, *Carbon*, 2009, **47**, 145-152
11. C. Zhu, S. Guo, Y. Fang and S. Dong, *ACS Nano*, 2010, **4**, 2429–2437.
12. D. Geng, S. Yang, Y. Zhanga , J. Yang, J. Liu, R. Li, T.-K. Sham, X. Sun, S. Ye and S. Knights, *Appl. Surf. Sci.*, 2011, **257**, 9193– 9198.
13. K. R. Lee, K. U. Lee, J. W. Lee, B. T. Ahn and S. I. Woo, *Electrochem. Commun.*, 2010, **12**, 1052–1055.
14. S. Yang, X. Feng, X. Wang and K. Millen, *Angew. Chem. Int. Ed.*, 2011, **50**, 5339 –5343.
15. J. Liang, Y. Jiao, M. Jaroniec and S. Z. Qiao, *Angew. Chem. Int. Ed.*, 2012, **51**, 11496 –11500.
16. J.-Y. Choi, D. Higgins and Z. Chen, *J. Electrochem. Soc.*, 2012, **159**, B86-B89.
17. R. I. Jafri, N. Rajalakshmi and S. Ramaprabhu, *J. Mater. Chem.*, 2010, **20**, 7114–7117.
18. N. Alexeyeva, E. Shulga, V. Kisand, I. Kink and K. Tammeveski, *J. Electroanal. Chem.*, 2010, **648**, 169-175.
19. M. Vikkisk, I. Kruusenberg, U. Joost, E. Shulga and K. Tammeveski, *Electrochim. Acta*, 2013, **87**, 709-716.

ARTICLE

20. M. Vikkisk, I. Kruusenberg, U. Joost, E. Shulga, I. Kink and K. Tammeveski, *Appl. Catal. B: Environ.*, 2014, **147**, 369-376.

21. S. Ratso, I. Kruusenberg, M. Vikkisk, U. Joost, E. Shulga, I. Kink, T. Kallio and K. Tammeveski, *Carbon*, 2014, **73**, 361-370.

22. M. Vikkisk, I. Kruusenberg, S. Ratso, U. Joost, E. Shulga, I. Kink, P. Rauwel and K. Tammeveski, *RSC Adv.*, 2015, **5**, 59495-59505.

23. V.V. Strelko, N.T. Kartel, I.N. Dukhno, V.S. Kuts, R.B. Clarkson and B. M. Odintsov, *Surface Science*, 2004, **548**, 281–290.

24. J. R. Pels, F. Kapteijn, J.A. Moulijn, Q. Zhu and K. M. Thomas, *Carbon*, 1995, **33**, 1641–1653.

25. S. v. Dommele, A. Romero-Izquirdo, R. Brydson, K. P. d. Jong and J. H. Bitter, *Carbon*, 2008, **46**, 138 –148.

26. D. Higgins, Z. Chen and Z. Chen, *Electrochim. Acta*, 2011, **56**, 1570–1575.

27. C. V. Rao, C. R. Cabrera and Y. Ishikawa, *J. Phys. Chem. Lett.*, 2010, **1**, 2622–2627.

28. S. Ni, Z. Li and J. Yang, *Nanoscale* 2012, **4**, 1184-1189.

29. L. Zhang and Z. Xia, *J. Phys. Chem. C* 2011, **115**, 11170–11176.

30. L. Yu, X. Pan, X. Cao, P. Hub and X. Bao, *Journal of Catalysis*, 2011, **282**, 183–190.

31. K. A. Kurak and A. B. Anderson, *J. Phys. Chem. C*, 2009, **113**, 6730–6734.

32. H. Kim, K. Lee, S. I. Woo and Y. Jung, *Phys. Chem. Chem. Phys.*, 2011, **13**, 17505–17510.

33. R. A. Sidik, A. B. Anderson, N. P. Subramanian, S. P. Kumaraguru and B. N. Popov, *J. Phys. Chem. B*, 2006, **110**, 1787-1793.

34. M.N. Groves, A.S.W. Chan, C. Malardier-Jugroot and M. Jugroot, *Chem. Phys. Lett.*, 2009, **481**, 214–219.

35. L. Zhang, J. Niu, L. Dai and Z. Xia, *Langmuir*, 2012, **28**, 7542–7550.

36. M. Ho Seo, S. Mook Choi, J. Kyo Seo, S. Hyo Noh, W. Bae Kim and B. Han, *App. Cat. B: Env.*, 2013, **129**, 163–171.

37. M. Ho Seo, S. Mook Choi, E. Ja Lim, I. Hye Kwon, J. Kyo Seo, S. Hyo Noh, W. Bae Kim and B. Han, *ChemSusChem*, 2014, **7**, 2609–2620.

38. M. Ho Seo, S. Mook Choi, D. Un Lee, W. Bae Kim and Z. Chen, *J. Power Sources*, 2015, **300**, 1-9.

39. V. Tripkovic, E. Skúlasona, S. Siahrostami, J. K. Nørskov and J. Rossmeisl, *Electrochimica Acta*, 2010, **55**, 7975–7981.

40. A. Michaelides and P. Hu, *J. Am. Chem. Soc.*, 2001, **123**, 4235–4242.

41. M. P. Hyman and J. W. Medlin, *J. Phys. Chem. B*, 2006, **110**, 15338–15344.

42. L. Qi, J. G. Yu and J. Li, *J. Chem. Phys.*, 2006, **125**, 8.

43. Y. Sha, T. H. Yu, Y. Liu, B. V. Merinov and W. A. Goddard III, *J. Phys. Chem. Lett.*, 2010, **1**, 856–861.

44. Y.-H. Li, T.-H. Hung and C.-W. Chen, *Carbon*, 2009, **47**, 850–855.

45. S. Peng and K. Cho, *Nano Lett.*, 2003, **3**, 513–517.

46. I. Kruusenberg, S. Ratso, M. Vikkisk, P. Kanninen, T. Kallio, A. M. Kannan and K. Tammeveski, *J. Power Sources*, 2015, **281**, 94-102.

47. I. Kruusenberg, J. Mondal, L. Matisen, V. Sammelselg and K. Tammeveski, *Electrochem. Commun.*, 2013, **33**, 18–22.

48. I. Kruusenberg, L. Matisen and K. Tammeveski, *J. Nanosci. Nanotechnol.*, 2013, **13**, 621–627.

49. Y. Kim, Y. Noh, E. Ja Lim, S. Lee, S. Mook Choi and W. B. Kim, *J. Mater. Chem. A*, 2014, **2**, 6976-6986.

50. H. Niwa, K. Horiba, Y. Harada, M. Oshima, T. Ikeda, K. Terakura, J. Ozaki and S. Miyata, *J. Power Sources*, 2009, **187**, 93-97.

51. D.H. Deng, X.L. Pan, L. Yu, Y. Cui, Y.P. Jiang, J. Qi, W.X. Li, Q. Fu, X.C. Ma, Q.K. Xue, G.Q. Sun and X.H. Bao, *Chem. Mater.*, 2011, **23**, 1188.

52. D. U. Lee, H. W. Park, D. Higgins, L. Nazar and Z. Chen, *J. Electrochem. Soc.*, 2013, **160**, F910-F915.

53. William S. Hummers Jr. and R. E. Offeman, *J. Am. Chem. Soc.*, 1958, **80**, 1339.

54. *Gaussian 09, Revision D.01,*
 M. J. Frisch, G. W. Trucks, H. B. Schlegel, G. E. Scuseria, M. A. Robb, J. R. Cheeseman, G. Scalmani, V. Barone, B. Mennucci, G. A. Petersson, H. Nakatsuji, M. Caricato, X. Li, H. P. Hratchian, A. F. Izmaylov, J. Bloino, G. Zheng, J. L. Sonnenberg, M. Hada, M. Ehara, K. Toyota, R. Fukuda, J. Hasegawa, M. Ishida, T. Nakajima, Y. Honda, O. Kitao, H. Nakai, T. Vreven, J. A. Montgomery, Jr., J. E. Peralta, F. Ogliaro, M. Bearpark, J. J. Heyd, E. Brothers, K. N. Kudin, V. N. Staroverov, T. Keith, R. Kobayashi, J. Normand, K. Raghavachari, A. Rendell, J. C. Burant, S. S. Iyengar, J. Tomasi, M. Cossi, N. Rega, J. M. Millam, M. Klene, J. E. Knox, J. B. Cross, V. Bakken, C. Adamo, J. Jaramillo, R. Gomperts, R. E. Stratmann, O. Yazyev, A. J. Austin, R. Cammi, C. Pomelli, J. W. Ochterski, R. L. Martin, K. Morokuma, V. G. Zakrzewski, G. A. Voth, P. Salvador, J. J. Dannenberg, S. Dapprich, A. D. Daniels, O. Farkas, J. B. Foresman, J. V. Ortiz, J. Cioslowski, and D. J. Fox, Gaussian, Inc., Wallingford CT, 2013.

55. J. J. P. Stewart, *J. Mol. Model.*, 2007, **13**, 1173-1213.

56. J. Rezac, J. Fanfrlík, D. Salahub and P. Hobza, *J. Chem. Theory Comput.*, 2009, **5**, 1749–1760.

57. M. J. McAllister, J.-L. Li, D. H. Adamson, H. C. Schniepp, A. A. Abdala, J. Liu, M. Herrera-Alonso, D. L. Milius, R. Car, R. K. Prud'homme and I. A. Aksay, *Chem. Mater.*, 2007, **19**, 4396–4404.

58. A. Celzard, J.F. Marêché and G. Furdin, *Prog. Mater Sci.*, 2005, **50**, 93-179.

59. D. Geng, Y. Chen, Y. Chen, Y. Li, R. Li, X. Sun, S. Yeb and S. Knights, *Energy Environ. Sci.*, 2011, **4**, 760-764.

60. G.-P. Dai, J.-M. Zhang and S. Deng, *Chem. Phys. Lett.*, 2011, **516**, 212-215.

61. K. N. Kudin, B. Ozbas, H. C. Schniepp, R. K. Prud'homme, I. A. Aksay and R. Car, *Nano Letters*, 2008, **8**, 36–41.

62. G. Wu, G. Cui, D. Li, P.-K. Shen and N. Lia, *J. Mater. Chem.*, 2009, **19**, 6581-6589.

63. T. Iwazaki, R. Obinata, W. Sugimoto and Y. Takasu, *Electrochem. Commun.*, 2009, **11**, 376-378.

64. G. Lalande, R. Cote, D. Guay, J. P. Dodelet, L. T. Weng and P. Bertrand, *Electrochim. Acta*, 1997, **42**, 1379-1388.

65. X. Li, H. Wang, J. T. Robinson, H. Sanchez, G. Diankov and H. Dai, *J. Am. Chem. Soc.*, 2009, **131**, 15939–15944.

66. G. Liu, X. Li, P. Ganesan and B. N. Popov, *Appl. Catal., B: Environ.*, 2009, **93**, 156–165.

67. Pels JR, Kapteijn F, Moulijn JA, Zhu Q and T. KM, *Carbon*, 1995, **33**, 1641-1653.

68. H. C. Choi, S. Y. Bae, W.-S. Jang and J. Park, *J. Phys. Chem. B*, 2005, **109**, 1683–1688.

69. T. Zhang and A. B. Anderson, *Electrochim. Acta*, 2007, **53**, 982–989.

70. A. B. Anderson, *ECS Transactions*, 2010, **28**, 1-17.

71. J. Rossmeisl, A. Logadottir and J. K. Nørskov, *Chem. Phys.*, 2005, **319**, 178–184.

72. J. K. Nørskov, J. Rossmeisl, A. Logadottir, L. Lindqvist, J. R. Kitchin, T. Bligaard and H. Jonsson, *J. Phys. Chem. B*, 2004, **108**, 17886-17892.

73. V. Viswanathan, H. A. Hansen, J. Rossmeisl and J. K. Nørskov, *ACS Catal.*, 2012, **2**, 1654–1660.

74. V. Viswanathan, H. A. Hansen, J. Rossmeisl and J. K. Nørskov, *J. Phys. Chem. Lett.* , 2012, **3**, 2948–2951.

75. J. Rossmeisl, J. K. Nørskov, C. D. Taylor, M. J. Janik and M. Neurock, *J. Phys. Chem. B*, 2006, **110**, 21833-21839.

76. E. Yeager, *J Mol. Catal.*, 1986, **38**, 5–25.

77. A.J. Bard and L. R. Faulkner, *Electrochemical Methods: Fundamentals and Application*, John Wiley & Sons, USA, 1980.